Electronic Supplementary Material (ESI) for Environmental Science: Nano.

Supporting information for

Fe/Mn nanoparticles encapsulated nitrogen-doped carbon nanotubes as peroxymonosulfate activator for acetamiprid degradation

Pijun Duan[a], Tengfei Ma, Yue Yue, Yanwei Li[b*], Xue Zhang, Yanan Shang[a], Baoyu Gao[a], Qingzhu Zhang, Qinyan Yue[a], Xing Xu[a*]

[a] Shandong Key Laboratory of Water Pollution Control and Resource Reuse, School of Environmental Science and Engineering, Shandong University, Jinan 250100, PR China

[b] Environment Research Institute, Shandong University, Jinan, 250100, P. R. China

Number of pages: 36
Number of appendix text: 6
Numbers of Figure: 19
Numbers of Table: 10

*Corresponding author: Tel.: +86-531-88361912; Fax: +86-531-88364513
E-mail: xuxing@sdu.edu.cn
*Corresponding author: Tel.: +86-531-88361912; Fax: +86-531-88364513
E-mail: lyw@sdu.edu.cn

Appendix S1

Characterization

Thermogravimetric analysis (TGA) was conducted on a thermogravimetric analysis instrument (TGA/DSC1 STARe system, METTLER-TOLEDO). Xray diffraction (XRD) patterns were acquired on a Bruker D8-Advanced X-ray instrument. Raman spectroscopy was performed on a WITec alpha 300RA+ system. Morphologies of the samples were revealed on a scanning electron microscope (FEI Verios XHR 460, SEM) with an energy dispersive spectrometer (EDS) and a transmission electron microscope (JEOL 2100, TEM). High angle annular dark field scanning TEM (HAADF-STEM) images and corresponding energy-dispersive Xray spectroscopy (EDX) elemental mapping were achieved by FEI Titan G2 80-200 TEM/STEM. X-ray photoelectron spectroscopy (XPS) was obtained with a Kratos AXIS Ultra DLD system under ultra-high vacuum (UHV) condition by monochromated Al-Kα X-rays. The specific surface area (SSA) and pore size distribution of the samples were determined by N_2 adsorption/desorption at -196 °C on a Micromertics Tristar 3000. Fourier Transform infrared (FTIR) was determined using the spectroscopy (Perkin–Elmer "Spectrum BX" spectrometer) with spectra recorded from 4000 to 400 cm^{-1}.

Appendix S2

Catalyst recycling and regenerating

The used catalyst was collected by filtrating and washed several times with distilled water to clean it. Then it was dried in an oven at 60 ^{o}C for 12 h. A new set of degradation test was done with another acetamiprid solution (2 mg/L) as well as the dried catalyst (0.1g/L) to measure the stability of FeMn@NCNTs. After the fourth set of catalytic degradation, a heated action at 350 °C for 1 h in air was used to regenerate the catalyst.

Appendix S3

Determination of free radical species

An EPR instrument (Bruker EMX/plus spectrometer, Germany) was serviced to detect the reactive free radicals generating from the N-doped biochar suspension with parameters as follows: center field 3460 G, sweep width 100 G, microwave frequency 9.71 GHz, microwave power 19.71 mW, modulation frequency 100 kHz, modulation amplitude of 1.0 G, sweep width of 100 G, sweep time of 83.97 s. Two spin-trapping agents, 5,5-dimethyl-1-pyrroline N-oxide (DMPO, > 99%, Aladdin) and 2,2,6,6-tetramethyl-4-piperidinol (TMP, > 99%, Aladdin), were employed to capture free radicals. Briefly, DMPO and TEMP were dissolved in phosphate buffer solutions (pH=7.4) to final concentrations of 80 mM and 50 mM, respectively. Then, 1 mL sample was withdrawn from FeMn@NCNTs suspension reaction system (acetamiprid concentration: 7.8 μM, FeMn@NCNTs dosage: 0.1 g/L, and PMS: 6.5 mM) and was filtered using 0.22 μm filter. DMPO or TMP solution (40 μL) was mixed with 40 μL filtered sample. A quartz capillary tube was used to suck up the mixed DMPO or TMP solution to detect corresponding signals from spin-trapping adducts in the EPR.

Appendix S4

Electrochemical measurement

All the electrochemical measurements were conducted at room temperature in a standard three-electrode electrochemical cell with a Ag/AgCl (4 M KCl) reference electrode, a platinum wire counter electrode and a catalyst-modified glassy carbon working electrode (0.196 cm^2, Pine Research Instrumentation, USA), and the electrolyte was a mixture of 0.1 M Na_2SO_4 and 6.5 mM PMS. Homogeneous catalyst ink was first prepared by sonication of 10 mg catalyst powder, 10 mg conductive carbon (Super P, Alfa Aesar), 0.1 mL Nafion solution (5 wt%, Sigma-Aldrich) and 1 mL absolute ethanol. Then, 7 μL of the as-prepared catalyst ink was pipetted onto the surface of the glassy carbon electrode, leading to a catalyst loading of ~0.325 mg cm^{-2}. The catalyst layer was dried in ambient air before use. All the electrochemical data were collected on a CHI 760E bipotentiostat. Cyclic voltammetry (CV) measurement was conducted between −1.0~1.0 V *vs*. Ag/AgCl at a scan rate of 50 mV s^{-1}. Electrochemical impedance spectra (EIS) were recorded at −0.3 V *vs*. Ag/AgCl within a frequency range from 10^5 to 10^{-1} Hz using an AC voltage at a 5 mV amplitude. Linear sweep voltammetry (LSV) was measured as the potential from -1.0~1.0 V (vs. Ag/AgCl) with a canning rate of 50 mV/s. Chronoamperometries were carried out at the bias of 0.0 V (vs. Ag/AgCl) with 50 mM Na_2SO_4 as supporting electrolyte.

Appendix S5

DFT calculations

The frontier electron density (FED) calculations were performed at the B3LYP/6-311G* level using the Gaussian 09 program. Frequency analysis after structural geometry optimizationwas used to confirm a true energy minimum on the potential energy surface. The HOMO and LUMO denotes the highest occupied molecular orbital and the lowest unoccupied molecular orbital, respectively[1, 2].

Employing the Vienna ab initio Simulation Package (VASP), all calculations were performed using Perdew–Burke–Ernzerhof (PBE) parametrization of generalized gradient approximation to density functional theory (DFT) with projector-augmented wave potentials. We used a plane wave basis set with an energy cut off of 400 eV. The unit cell sizes for pyrrolic, pyridinic, and graphitic N-doped graphene are 25 × 25 × 15 Å. The atoms were relaxed fully until the force acting on each atom was less than 0.02 eV/Å. van der Waals (vdW) interaction was taken into account at the DFT-D3 level as proposed by Grimme. The adsorption energy is defined as

$$E_{ads} = E_{total} - E_{surf} - E_{PMS}$$

where E_{total}, E_{surf}, and E_{PMS} denote the total energy of surface with PMS, surface, and PMS, respectively.

Appendix S6

In general, $SO_4^{\bullet-}$ is vulnerable to being scavenged by halogen ions such as Cl^-, because $SO_4^{\bullet-}$ can oxidize Cl^- to chlorine radicals ($Cl^{\bullet}$), which presents a lower redox

potential for organic mineralization and can react with organics to form refractory chloride [3].

$SO_4^{\bullet-} + Cl^- \rightarrow SO_4^{2-} + Cl\bullet$ $k = 3.0 \times 10^8\ M^{-1}\ s^{-1}$ (1)

$SO_4^{2-} + Cl^{\bullet} \rightarrow SO_4^{\bullet-} + Cl^-$ $k = 2.5 \times 10^8\ M^{-1}\ s^{-1}$ (2)

$Cl\bullet + H_2O \rightarrow ClOH\bullet^- + H^+$ $k = 2.5 \times 10^5\ M^{-1}\ s^{-1}$ (3)

$ClOH\bullet^- + H^+ \rightarrow Cl\bullet + H_2O$ $k = 2.1 \times 10^{10}\ M^{-1}\ s^{-1}$ (4)

$ClOH\bullet^- + Cl^- \rightarrow Cl_2\bullet^- + OH^-$ $k = 1.0 \times 10^4\ M^{-1}\ s^{-1}$ (5)

$Cl\bullet + OH^- \rightarrow ClOH\bullet^-$ $k = 1.8 \times 10^{10}\ M^{-1}\ s^{-1}$ (6)

$Cl\bullet + Cl^- \rightarrow Cl_2\bullet^-$ $k = 8.5 \times 10^9\ M^{-1}\ s^{-1}$ (7)

$Cl_2\bullet^- + Cl\bullet \rightarrow Cl_2 + Cl^-$ $k = 2.1 \times 10^9\ M^{-1}\ s^{-1}$ (8)

$Cl\bullet + Cl\bullet \rightarrow Cl_2$ $k = 8.8 \times 10^7\ M^{-1}\ s^{-1}$ (9)

$SO_4\bullet^- + HCO_3^- \rightarrow HCO_3\bullet + SO_4^{2-}$ $k = 2.8 \times 10^6\ M^{-1}\ s^{-1}$ (10)

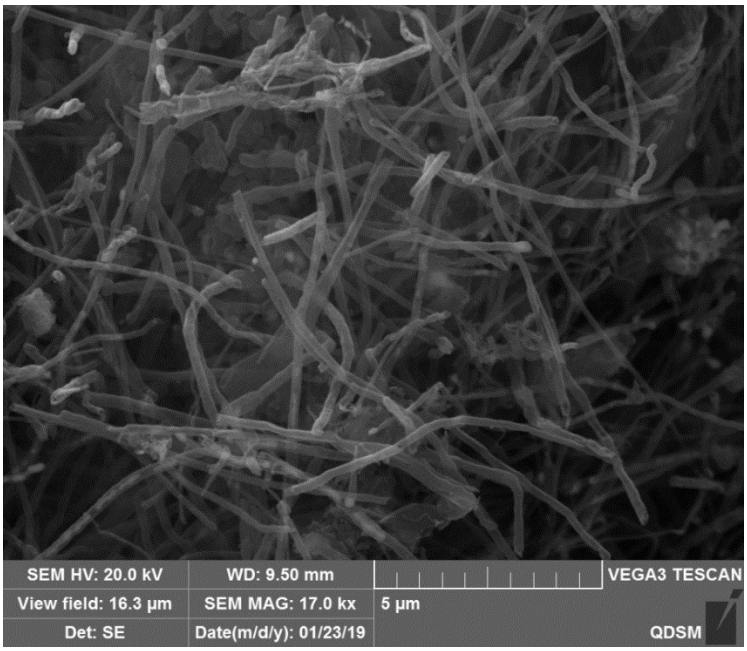

Fig. S1 SEM of FeMn@NCNTs 900

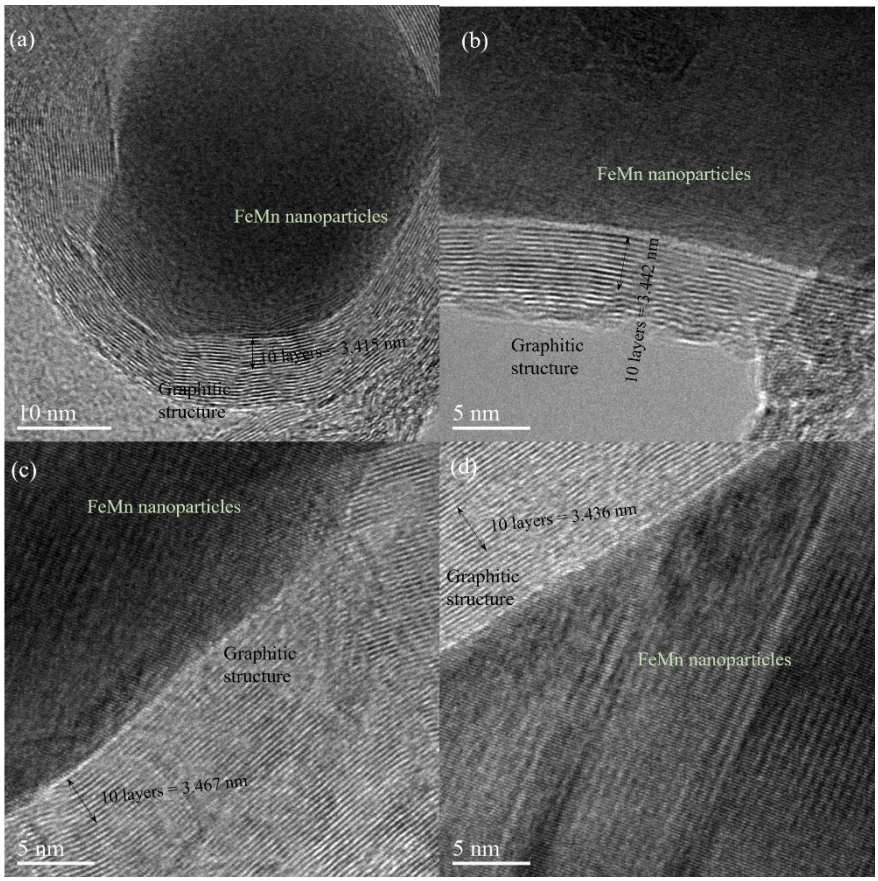

Fig. S2 (a) TEM of FeMn@NCNTs 600 (10 nm); (b) TEM of FeMn@NCNTs 750 (5 nm); (c) TEM of FeMn@NCNTs 900 (5 nm); (d) TEM of FeMn@NCNTs 1050 (5 nm)

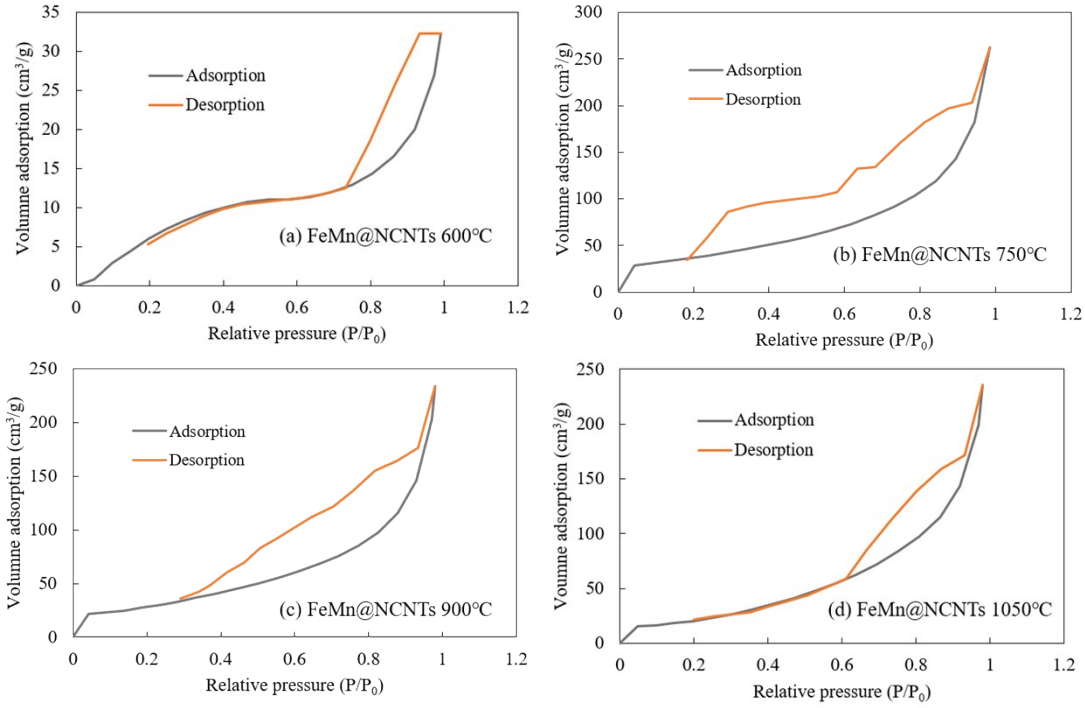

Fig. S3 N_2 adsorption/desorption of multiple FeMn@NCNTs

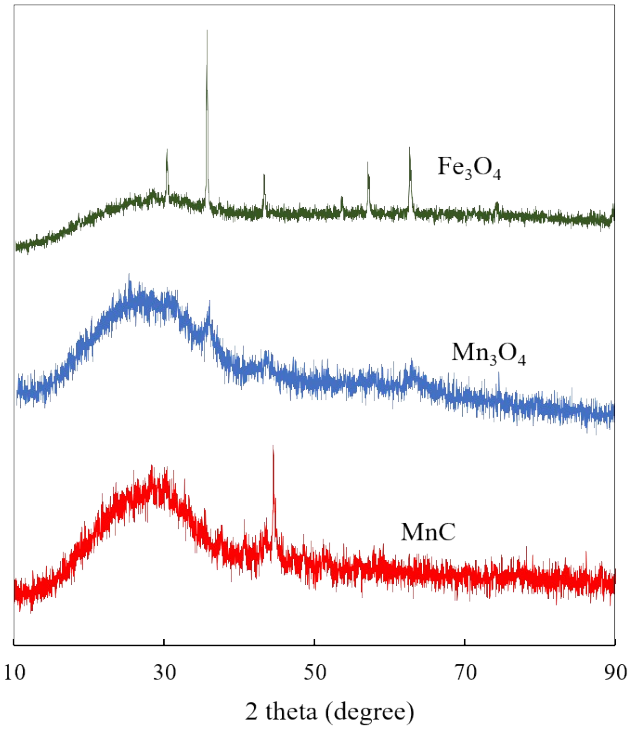

Fig. S4 XRD patterns of Fe_3O_4, Mn_3O_4, MnC nanoparticles

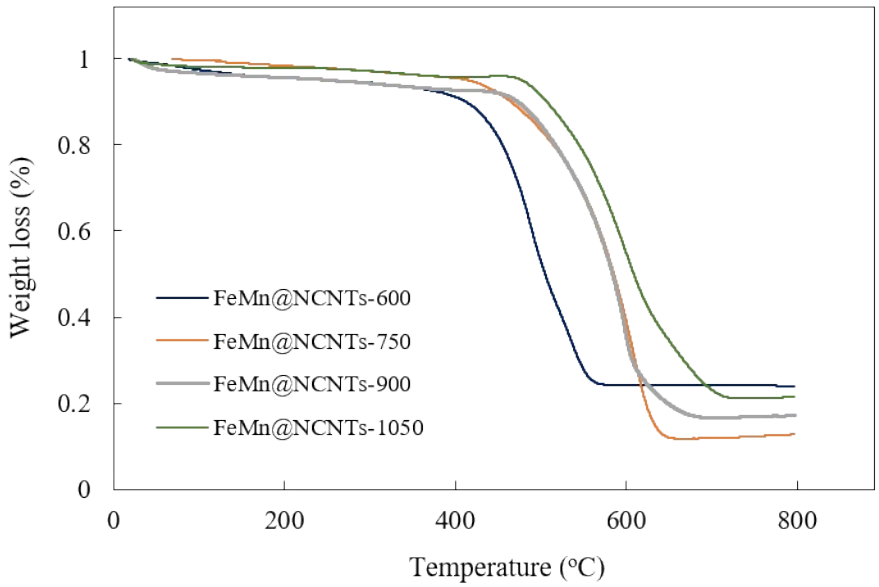

Fig. S5 TGA of multiple FeMn@NCNTs derived from different pyrolysis temperatures

The TGA plots of FeMn@NCNTs showed a mild weight loss below 450 °C, which can be assigned to the removal and destruction of the labile oxygenated functional groups on the carbon surface, such as –OH and C=O in the forms of H_2O, CO and CO_2.

The weight decreased dramatically in the range from 400 °C to 650 °C, which was ascribed to (i) the oxidation and decomposition of the NCNTs, and (ii) possible transformation of Fe/Mn nanoparticles into Fe/Mn oxides [4]. When the temperature reached 650-700 °C, the weight of the samples remained unchanged, and almost no weight loss occurred beyond this temperature. Stable weight percentages of 23.92%, 12.76%, 17.11% and 21.55% were achieved for FeMn@NCNTs-600, FeMn@NCNTs-750, FeMn@NCNTs-900 and FeMn@NCNTs-1050, respectively. It is known that the weight loss rate of CNTs filled with ferromagnetic species always decreases with increasing temperature because of the destruction of the tube walls that provide protection to the inner filled metal, which results in the formation of metal oxides [4]. It is deduced that a point of inflection would exist in the TGA curve. However, the curves of the FeMn@NCNTs nanocomposites were relatively smooth, proving that the Fe/Mn nanoparticles encapsulated inside the nanotubes were oxidized by air simultaneously with the tube walls.

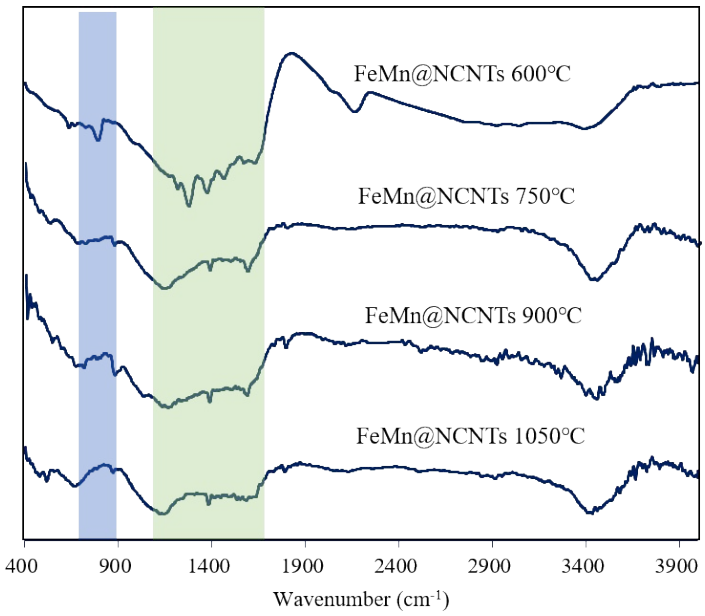

Fig. S6 FTIR spectra of multiple FeMn@NCNTs

FTIR spectrum of FeMn@NCNTs-600 indicated the emergence of various peaks at 1680, 1360–1460 and 750 cm^{-1}. These peaks can be ascribed to the N-based moieties such as -NH_2, N-H bending, C-N stretching, and N-H out of plane bending, respectively [5]. The N-based moieties are decomposed and coalesced into the carbon lattice at higher temperature to form various N configurations including pyridinic N, pyrrolic N and graphitic N [6].

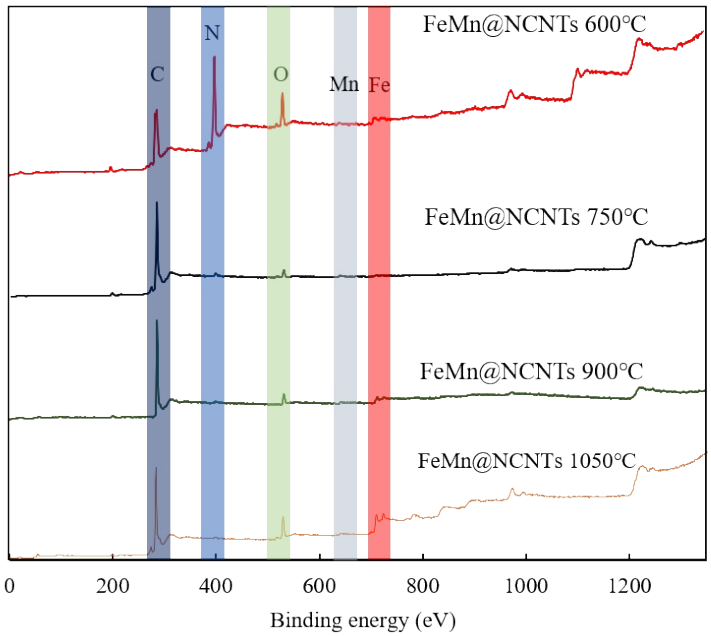

Fig. S7 XPS spectra of multiple FeMn@NCNTs

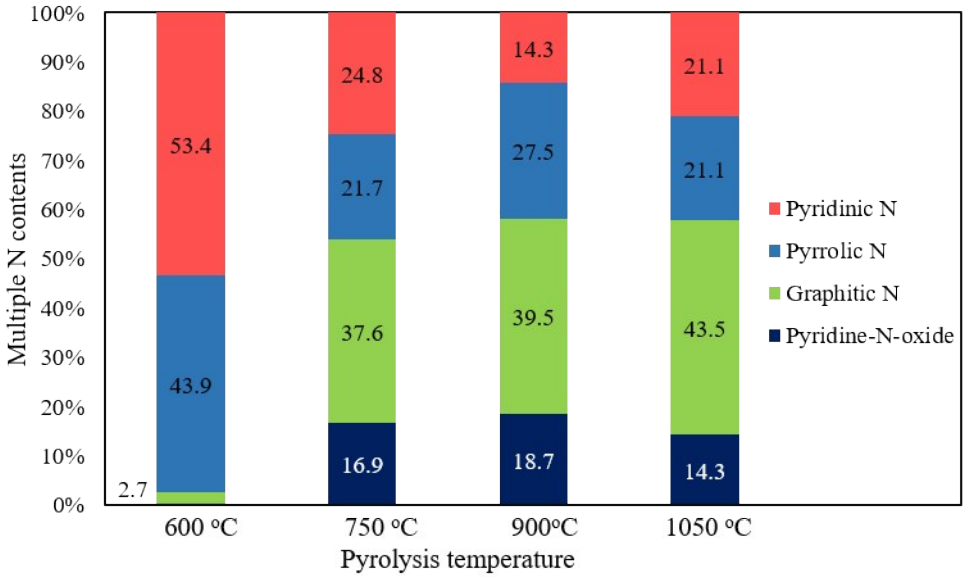

Fig. S8 Variation of N amounts in multiple FeMn@NCNTs derived from different pyrolysis temperatures

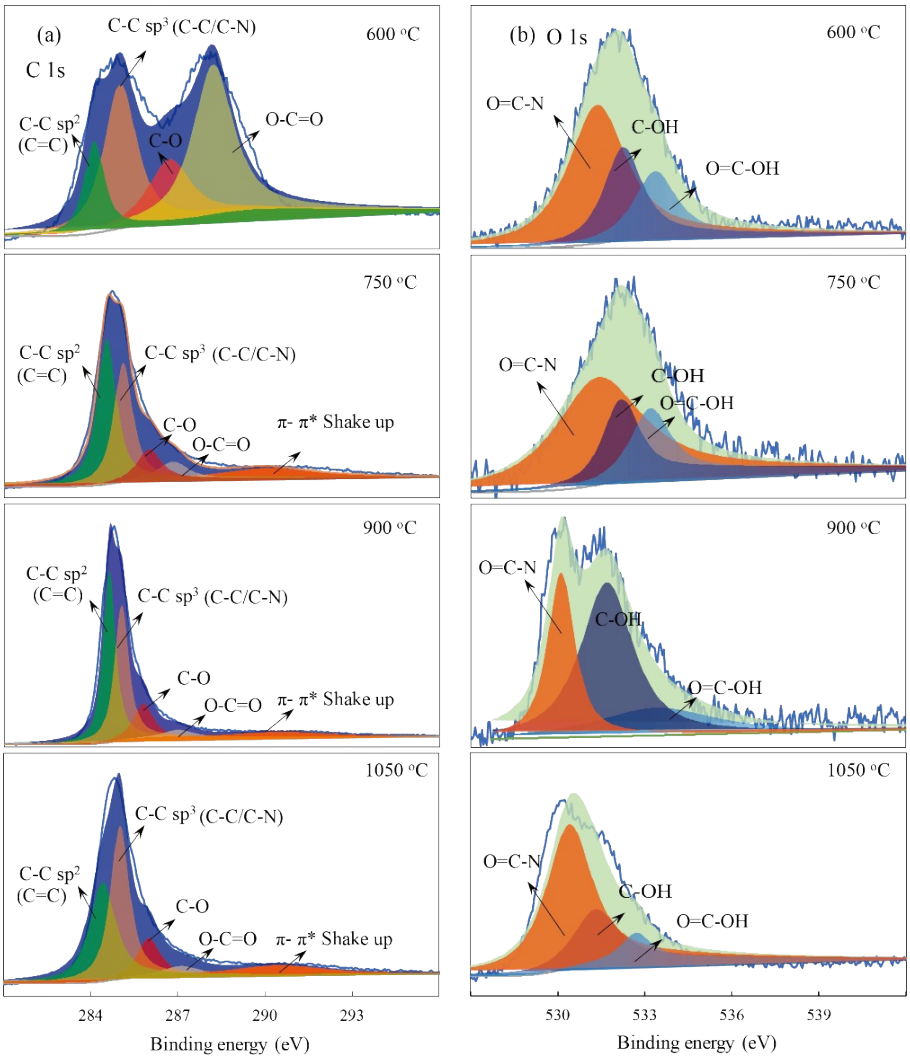

Fig. S9 (a) C 1s and (b) O 1s of multiple FeMn@NCNTs prepared at different pyrolysis temperatures

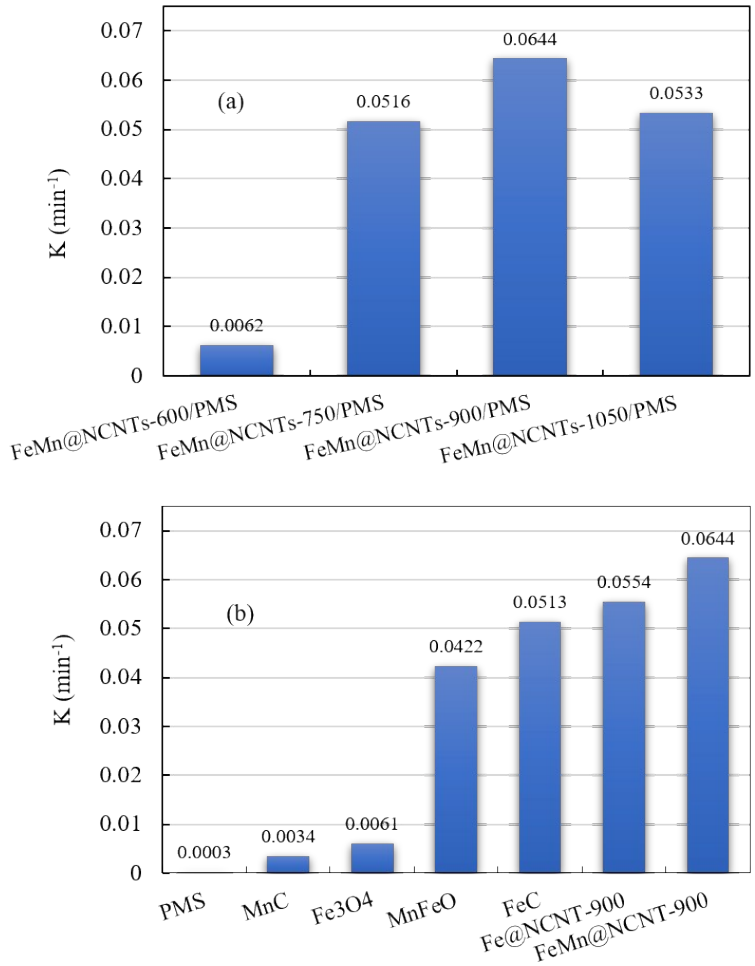

Fig. S10 Reaction rate constants of (a) multiple FeMn@NCNTs and (b) other Fe/Mn catalysts

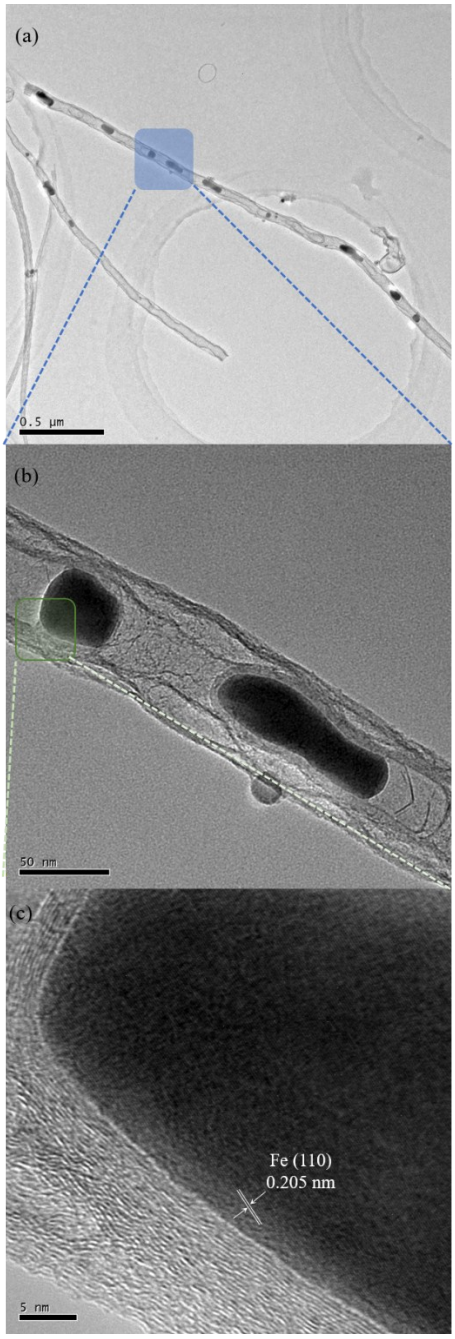

Fig. S11 TEM of Fe@NCNTs (a)500 nm; (b) 50 nm; (c) 5 nm

The iron nanoparticle wrapped in carbon is confirmed by the HRTEM. The lattice spacing could be measured about 0.205 nm, which is close to the standard value of 0.204 nm, corresponding to the [110] plane of metallic iron [7].

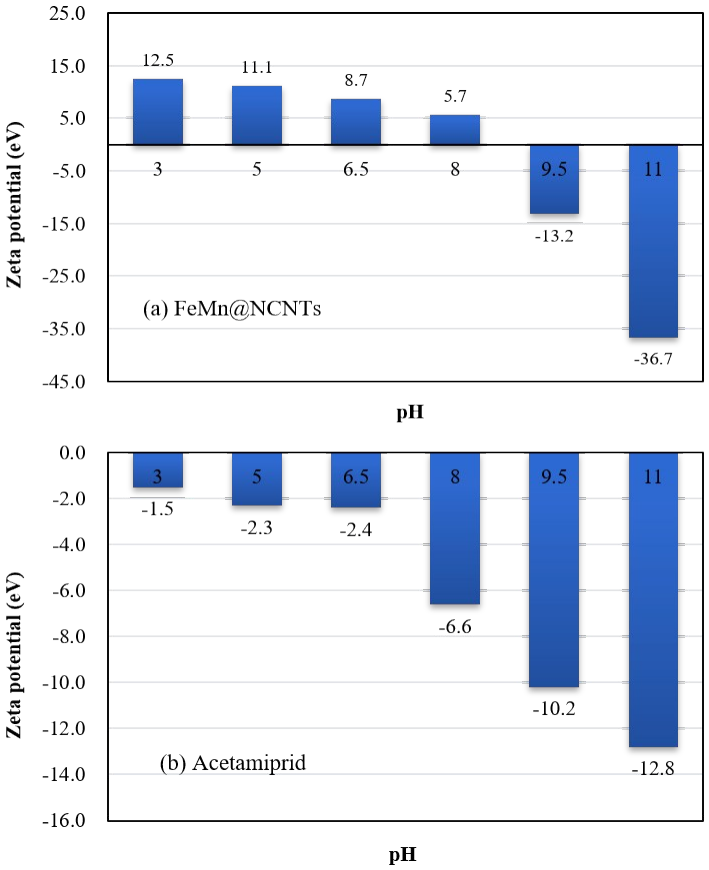

Fig. S12 Zeta potentials of (a) FeMn@NCNTs and (b) acetamiprid at different pH

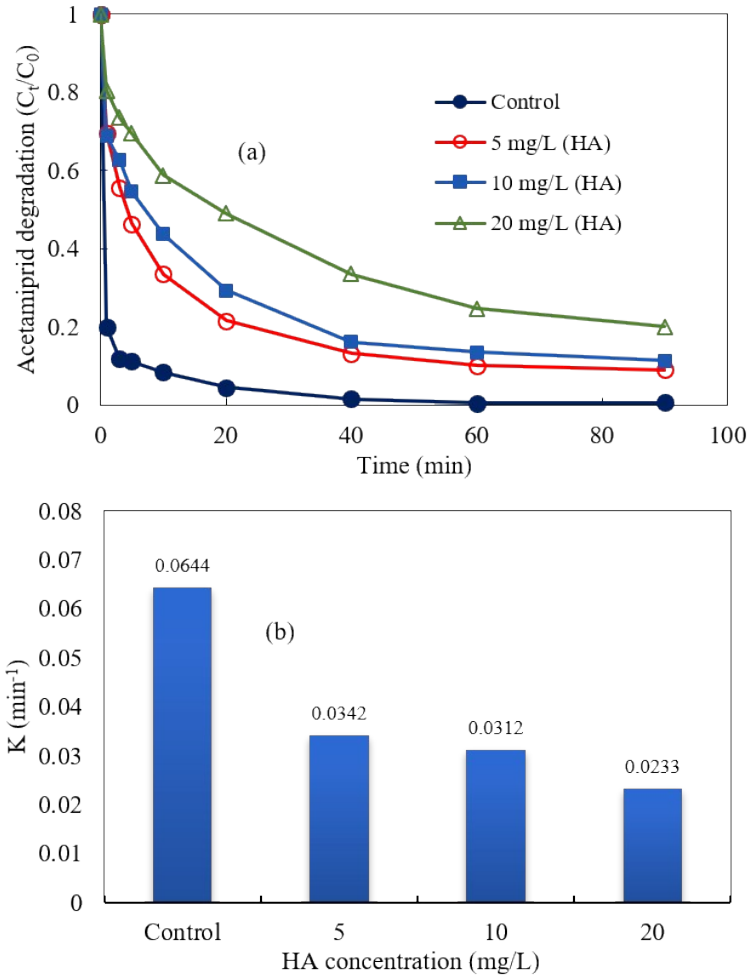

Fig. S13 (a) Acetamiprid degradation by FeMn@NCNTs with different concentrations of HA; (b) degradation rate

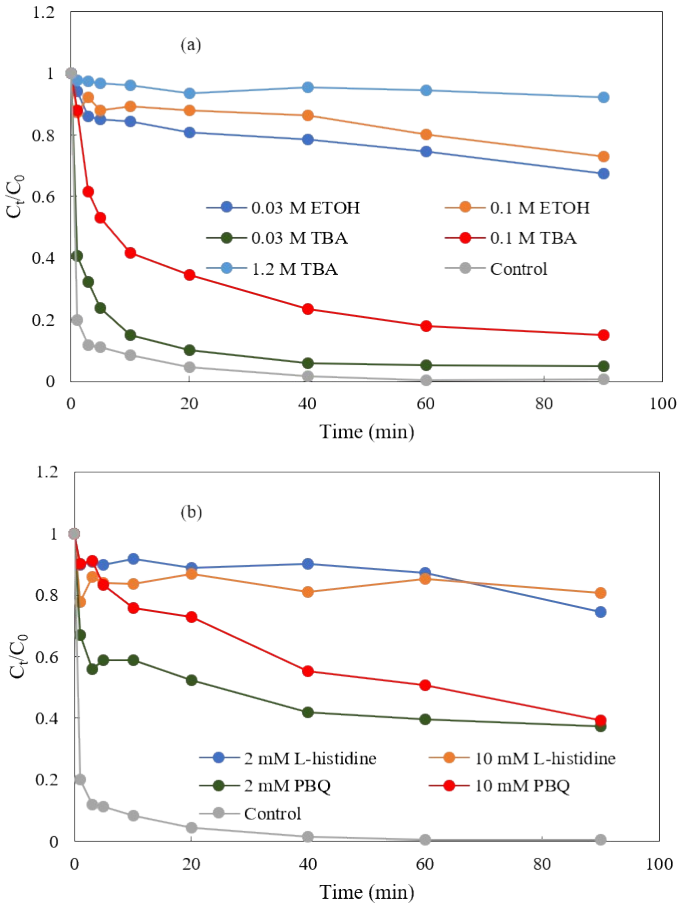

Fig. S14 Acetamiprid degradation in Fe@NCNT/PMS system in the presence of different scavenger (a) EtOH and TBA, (c) $_L$-histidine and p-BQ. (Fe@NCNT dosage: 0.1 g/L; $[PMS]_0$: 6.5 mM; $[acetamiprid]_0$: 7.8 μM)

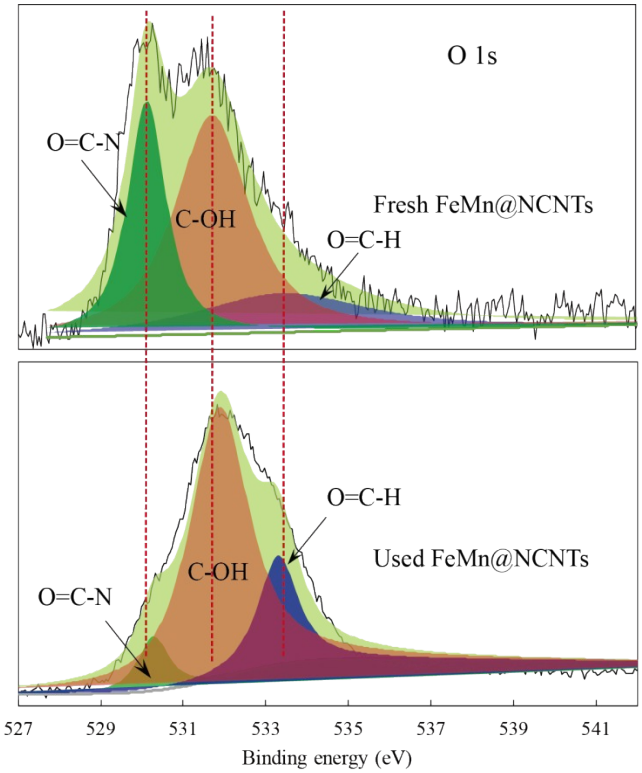

Fig. S15 O 1s spectra of fresh FeMn@NCNTs and used FeMn@NCNTs

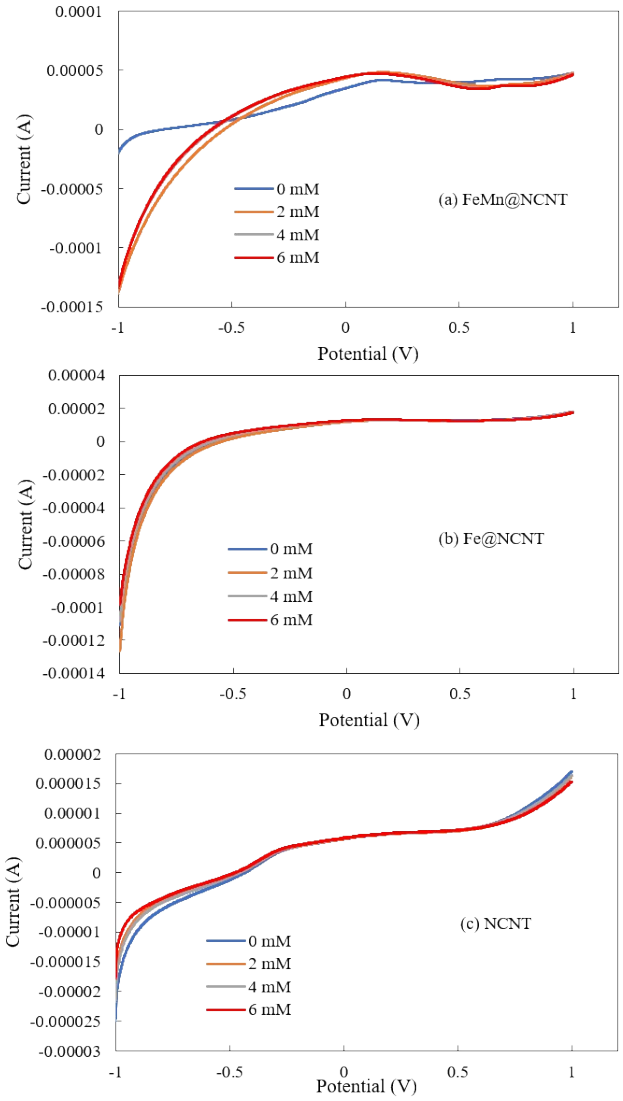

Fig. S16 LSV curves were measured at the range of -1.0-1.0 V vs. Ag/AgCl with (a) FeMn@NCNTs, (b) Fe@NCNTs and (c) NCNTs as catalyst. Conditions: scanning rate of 50 mV/s, 50 mM Na_2SO_4 as electrolyte, PMS concentration 0-6 mM.

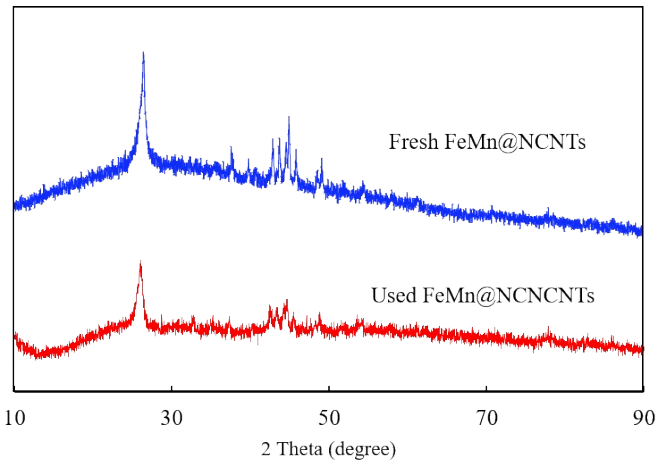

Fig. S17 XRD pattern of fresh/used used FeMn@NCNT-900

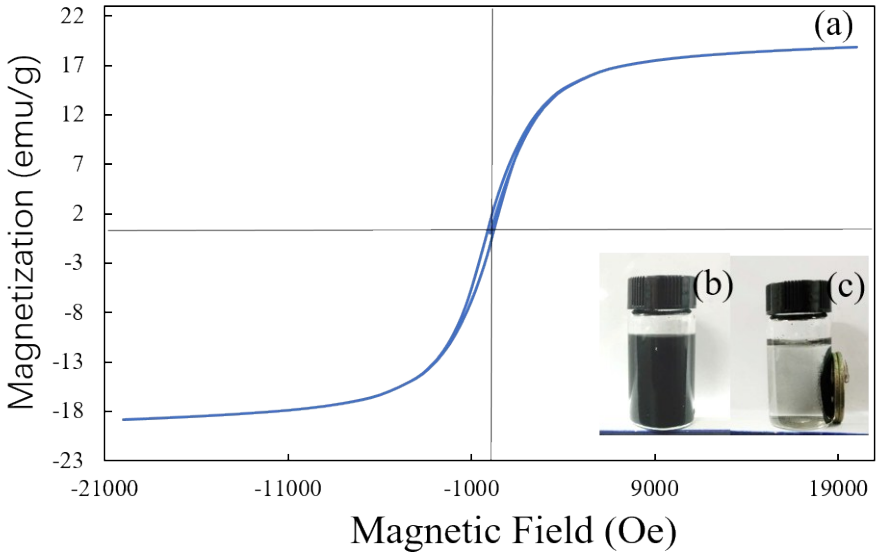

Fig. S18 (a) Hysteresis loops measured at 300 K of FeMn@NCNT-900; the photography that (b) FeMn@NCNT-900 in aqueous solution was attracted by magnet and (c) without magnet attracting

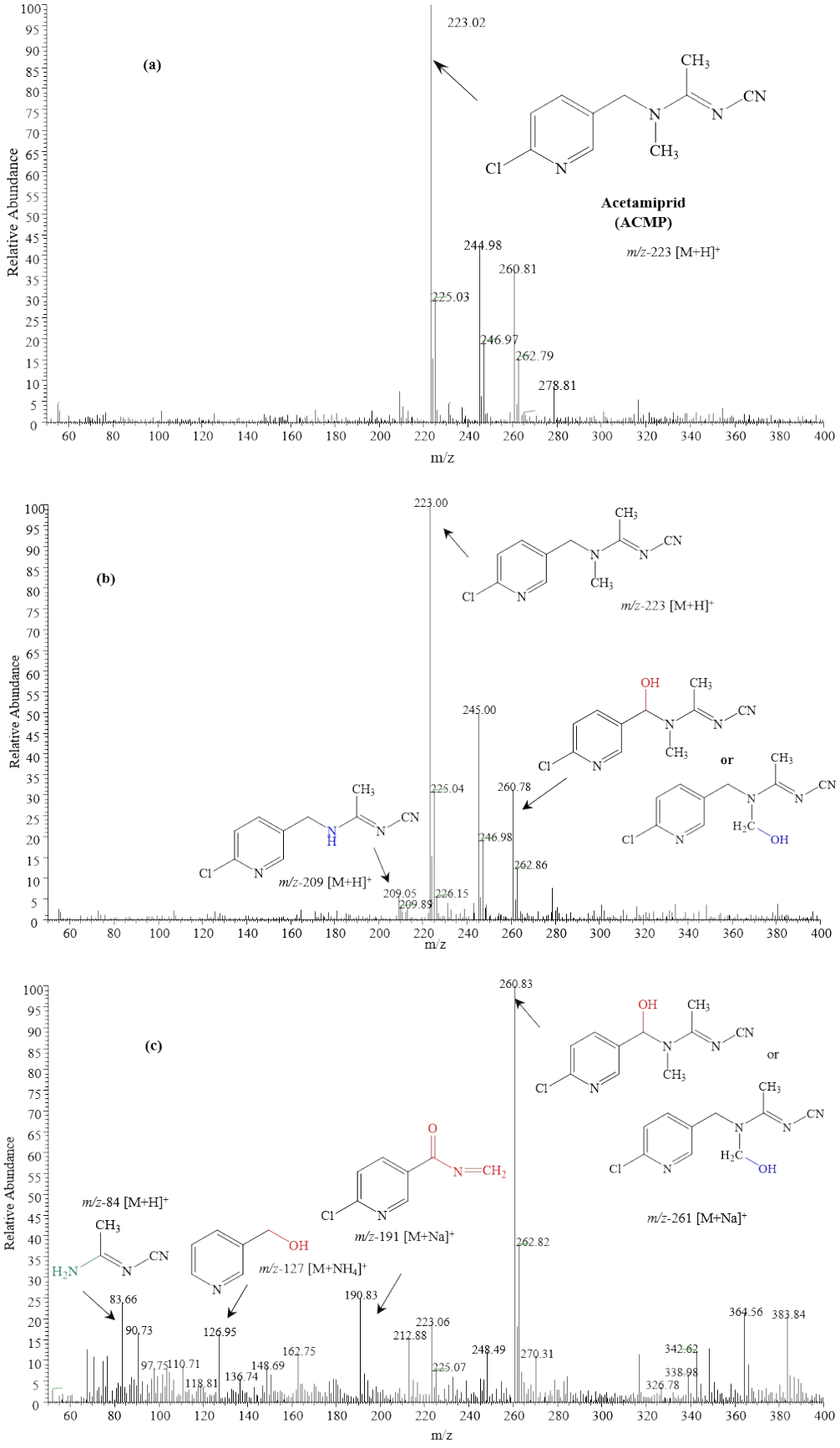
(a)
223.02
Acetamiprid
(ACMP)
m/z-223 [M+H]+
244.98
260.81
225.03
246.97
262.79
278.81
Relative Abundance
m/z
(b)
223.00
m/z-223 [M+H]+
245.00
225.04
260.78
246.98
262.86
209.05
209.89
226.15
m/z-209 [M+H]+
or
(c)
260.83
m/z-261 [M+Na]+
m/z-84 [M+H]+
m/z-127 [M+NH4]+
m/z-191 [M+Na]+
83.66
90.73
97.75
110.71
118.81
126.95
136.74
148.69
162.75
190.83
212.88
223.06
225.07
248.49
262.82
270.31
326.78
338.98
342.62
364.56
383.84

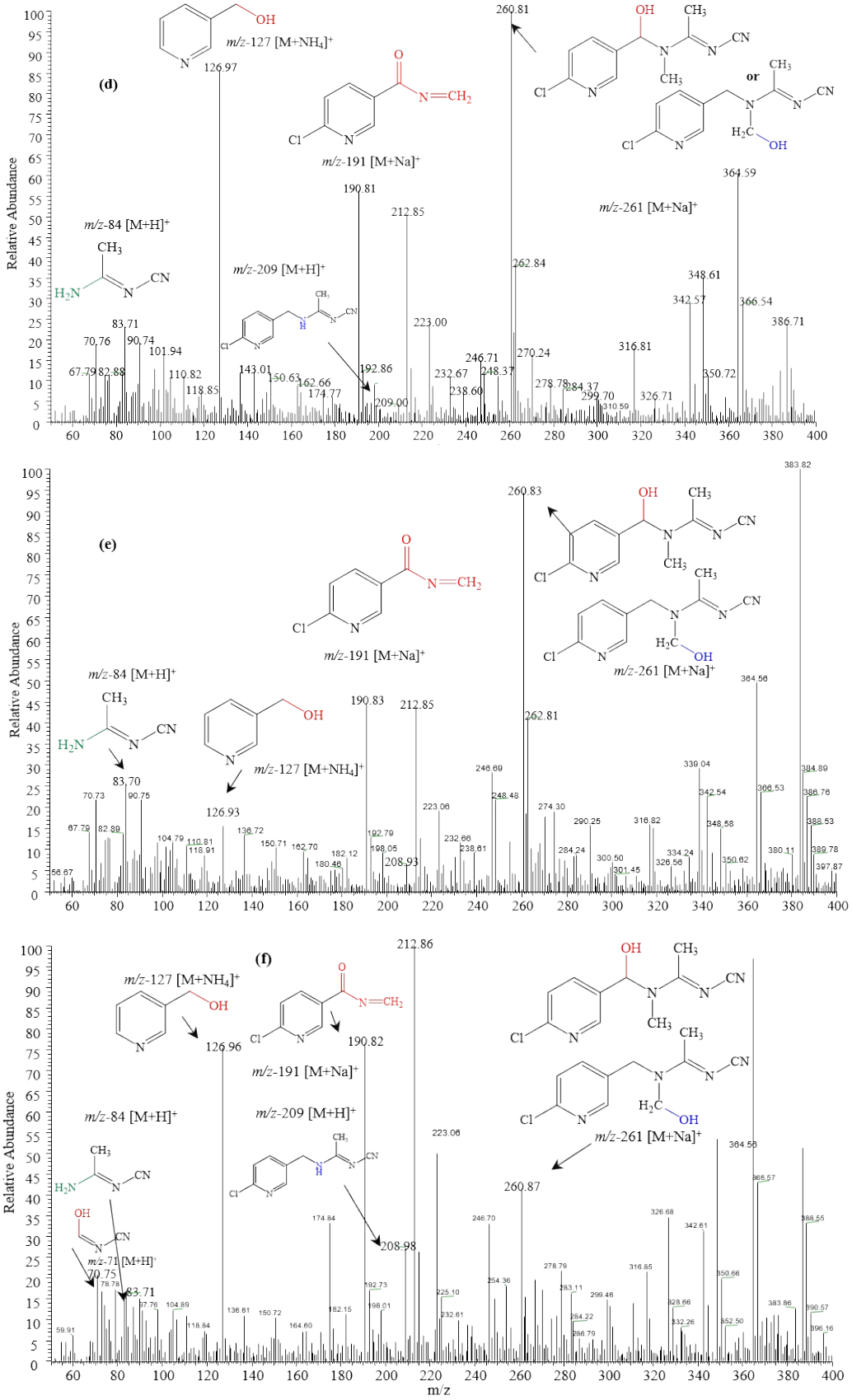

Fig. S19 LC-MS of ACMP solution (a) before catalytic reaction; (b) after 1 min catalytic reaction; (c) after 5 min catalytic reaction; (d) 10 min; (e) 30 min; (f) 60 min (The concentration of ACMP in LC-MS tests was 10 times higher than that in catalytic tests)

Table S1 Surface morphology of different FeMn@NCNTs

Materials	BET surface area (m^2/g)	Average pore diameter (nm)	Pore volume (cm^3/g)
FeMn@NCNTs-600	47.6	4.10	0.050
FeMn@NCNTs-750	108.1	13.43	0.363
FeMn@NCNTs-900	134.5	12.07	0.406
FeMn@NCNTs-1050	86.4	16.85	0.364

Table S2 Element at% of multiple FeMn@NCNTs

Catalysts	Element atomic %				
	C1s	N1s	O1s	Mn2p	Fe2p
FeMn@NCNTs-600	53.76	35.57	9.00	0.51	1.16
FeMn@NCNTs-750	92.32	3.23	3.39	0.52	0.54
FeMn@NCNTs-900	88.78	2.66	6.03	0.63	1.91
FeMn@NCNTs-1050	83.86	1.55	9.67	0.58	4.33

Table S3 XPS C 1s data of multiple FeMn@NCNTs

Catalysts		C-C sp^2	C-C sp^3	C-O	O-C=O	π-π* shake up
FeMn@NCNTs-600	BE	284.1	285.0	286.7	288.2	-
	at %	12.4	30.1	17.5	39.9	-
FeMn@NCNTs-750	BE	284.5	285.1	286.0	286.8	290.1
	at %	39.2	31.6	10.2	7.2	11.8
FeMn@NCNTs-900	BE	284.6	285.1	285.8	287.0	290.5
	at %	39.8	35.6	12.4	4.1	8.1
FeMn@NCNTs-1050	BE	284.4	285.0	286.0	287.1	290.5
	at %	34.3	38.7	11.5	4.6	10.9

Table S4 XPS O 1s data of multiple FeMn@NCNTs

Catalysts		O=C-N	C-OH	O=C-H
FeMn@NCNTs-600	BE	531.4	532.3	533.3
	at %	56.4	24.9	18.7
FeMn@NCNTs-750	BE	531.4	532.2	533.3
	at %	62.7	19.4	17.9
FeMn@NCNTs-900	BE	530.5	531.8	533.3
	at %	28.4	51.8	19.8
FeMn@NCNTs-1050	BE	530.3	531.7	532.9
	at %	68.1	24.3	7.6

Table S5 Element at% of fresh FeMn@NCNTs and used FeMn@NCNTs

Catalysts	Element atomic %				
	C1s	N1s	O1s	Mn2p	Fe2p
Fresh FeMn@NCNTs-900	88.78	2.66	6.03	0.63	1.91
Used FeMn@NCNTs-900	83.74	2.29	11.86	0.58	1.54

Table S6 XPS Fe 2p data of fresh FeMn@NCNTs and used FeMn@NCNTs

Catalysts		Fe $2p_{3/2}$		
		Oct. Fe(II)	Oct. Fe(III)	Tet. Fe(III)
Fresh FeMn@NCNTs-900	BE	710.3	711.3	713.2
	at %	7.6	34.4	58.0
Used FeMn@NCNTs-900	BE	710.3	711.3	713.3
	at %	5.9	45.9	48.2
Catalysts		Mn $2p_{3/2}$		
		Mn(II)	Mn(III)	Mn(IV)
Fresh FeMn@NCNTs-900	BE	641.0	642.2	643.5
	at %	38.2	25.3	36.5
Used FeMn@NCNTs-900	BE	641.1	642.2	643.6
	at %	22.7	34.0	43.3

Table S7 XPS N 1s data of fresh FeMn@NCNTs and used FeMn@NCNTs

Catalysts		Pyridinic N	Pyrrolic N	Graphitic N	Pyridinic N-oxide
Fresh	BE	398.6	400.5	401.6	406.0
FeMn@NCNTs-900	at %	14.3	27.5	39.5	18.7
Used	BE	398.5	399.8	401.6	406.6
FeMn@NCNTs-900	at %	11.6	43.5	28.2	16.7

Table S8 XPS O 1s data of fresh FeMn@NCNTs and used FeMn@NCNTs

Catalysts		O=C-N	C-OH	O=C-H
Fresh FeMn@NCNTs-900	BE	530.5	531.8	533.3
	at %	28.4	51.8	19.8
Used FeMn@NCNTs-900	BE	530.3	531.7	532.9
	at %	7.7	72.8	19.5

Table S9 The adsorption energies (ΔE_{ads}) in terms of the relaxed atom structure of a PMS

molecule adsorbed on different positions of carbon models

	E_{total}/eV	E_{surf}/eV	E_{PMS}/eV	E_{ads}/eV
Graphitic N	-482.13	-442.01	-36.50	-3.62
Pyridine N	-468.49	-430.14	-36.50	-1.85
Pyrrolic N	-467.90	-429.80	-36.50	-1.60

Table S10. Hypothetical chemical structures of the intermediates

m/z	Molecular formula	Proposed structure
m/z-223 $[M+H]^+$	$C_{10}H_{12}ClN_4^+$	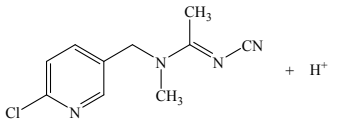
m/z-261 $[M+Na]^+$	$C_{10}H_{11}ClN_4ONa^+$	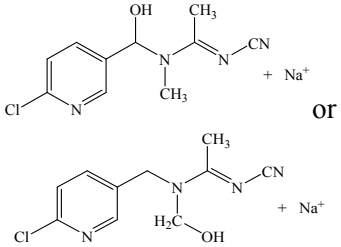 or
m/z-209 $[M+H]^+$	$C_9H_{10}ClN_4^+$	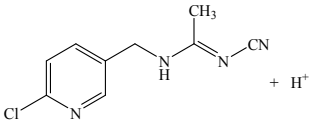
m/z-175 $[M+H]^+$	$C_9H_{11}N_4^+$	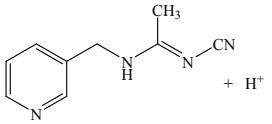
m/z-168 $[M+Na]^+$	$C_7H_5N_2OClNa^+$	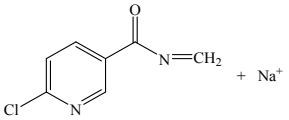
ACMP-127 (m+18)	$C_6H_{11}N_2O^+$	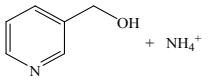
ACMP-84 (m+1)	$C_3H_6N_3^+$	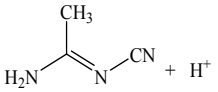

References

1. X. Pan, J. Chen, N. Wu, Y. Qi, X. Xu, J. Ge, X. Wang, C. Li, R. Qu, V. K. Sharma and Z. Wang, Degradation of aqueous 2,4,4'-Trihydroxybenzophenone by persulfate activated with nitrogen doped carbonaceous materials and the formation of dimer products, *Water research*, 2018, **143**, 176-187.
2. L. Lyu, G. Yu, L. Zhang, C. Hu and Y. Sun, 4-Phenoxyphenol-Functionalized Reduced Graphene Oxide Nanosheets: A Metal-Free Fenton-Like Catalyst for Pollutant Destruction, *Environmental science & technology*, 2017, **52**, 747-756.
3. L. Tang, Y. Liu, J. Wang, G. Zeng, Y. Deng, H. Dong, H. Feng, J. Wang and B. Peng, Enhanced activation process of persulfate by mesoporous carbon for degradation of aqueous organic pollutants: Electron transfer mechanism, *Applied Catalysis B: Environmental*, 2018, **231**, 1-10.
4. W. Tian, H. Zhang, Z. Qian, T. Ouyang, H. Sun, J. Qin, M. O. Tadé and S. Wang, Bread-making synthesis of hierarchically Co@C nanoarchitecture in heteroatom doped porous carbons for oxidative degradation of emerging contaminants, *Applied Catalysis B: Environmental*, 2018, **225**, 76-83.
5. W.-D. Oh, L.-W. Lok, A. Veksha, A. Giannis and T.-T. Lim, Enhanced photocatalytic degradation of bisphenol A with Ag-decorated S-doped g-C3N4 under solar irradiation: Performance and mechanistic studies, *Chemical Engineering Journal*, 2018, **333**, 739-749.
6. W.-D. Oh, G. Lisak, R. D. Webster, Y.-N. Liang, A. Veksha, A. Giannis, J. G. S. Moo, J.-W. Lim and T.-T. Lim, Insights into the thermolytic transformation of lignocellulosic biomass waste to redox-active carbocatalyst: Durability of surface active sites, *Applied Catalysis B: Environmental*, 2018, **233**, 120-129.
7. B. Liu, W. Dai, Z. Liang, J. Ye and L. Ouyang, Fe/N/C carbon nanotubes with high nitrogen content as effective non-precious catalyst for oxygen reduction reaction in alkaline medium, *International Journal of Hydrogen Energy*, 2017, **42**, 5908-5915.